Journal of Marine Research, 53, 1–22, 1995

Journal of
MARINE RESEARCH

Volume 53, Number 1

Dispersion of wind-induced inertial waves by a barotropic jet

by P. Klein[1] and A. M. Treguier[1]

ABSTRACT

This note attempts to reinterpret previous results on the dispersion of wind-induced inertial waves by a geostrophic barotropic jet in the ocean. The approach is to consider the jet vorticity influence on the different baroclinic modes using a vertical normal mode expansion. Numerical and analytical analysis of the linear equations shows that vorticity effects on a single baroclinic mode strongly depend on the ratio of its Rossby radius and the length scale of the geostrophic vorticity: trapping of the near-inertial energy occurs when this ratio is small. When this ratio is of order one, inertial waves are almost unaffected by the geostrophic vorticity because dispersion efficiently overcomes the jet vorticity effects. A 2-D primitive-equation model is used to examine the scattering of wind-induced inertial waves in realistic situations. Results indicate that contribution of the lowest baroclinic modes, unaffected by the jet vorticity, explain some striking features reported in previous studies as the downward phase propagation of near-inertial waves in the positive vorticity region.

1. Introduction

Several studies have shown that the space-time spectrum of near-inertial motions is strongly modulated by ocean fronts and geostrophic shear. Kunze (1985) demonstrates that the vorticity ζ associated with a geostrophic jet shifts the near-inertial

1. Laboratoire de Physique des Oceans, IFREMER, B.P. 70, 29280 Plouzane, France.

wave frequency from the Coriolis value f to an effective frequency $f_e \approx f + \zeta/2$. As a result phase differences accumulate in inertial waves within the jet, which leads to a spatial variability of these waves characterized by a wavenumber $k \approx -t\nabla\zeta/2$. Because of this evolving spatial variability, near-inertial waves are generally trapped within the negative vorticity region.

Such evolving spatial variability is particularly relevant to the dispersion of an initially large-scale mixed layer inertial wave field resulting from the passage of a rapidly propagating synoptic atmospheric front. To address this question Rubenstein and Roberts (1986) used a linearized primitive-equations (PE) model to examine the scattering of an initially homogeneous wind-induced inertial flow contained within a 50 m deep mixed layer by a geostrophic barotropic jet. They found that a large part of the inertial energy remains within the mixed layer, this energy being rapidly dispersed away from the positive vorticity region and partially trapped within the negative vorticity region. Only some inertial energy propagates within the stratified interior, mainly in the negative vorticity region. Wang (1991), using a PE model, examined the propagation of wind-induced inertial waves in the Subtropical Front and obtained results somewhat different from Rubenstein and Roberts (1986). His mixed-layer is deep (≈ 100 m) and the geostrophic jet is baroclinic (300 m deep). His results clearly show an inertial energy depletion within the mixed layer in the whole jet area and two distinct inertial energy maxima below the mixed layer: one deep maximum at the base of the thermocline in the negative vorticity region and a subsurface maximum at the top of the thermocline in the positive vorticity region. Moreover Wang reported an anomalously low frequency of the near-inertial waves in the positive vorticity region. As a consequence the phase propagation is downward in this region whereas it is upward in the negative vorticity region.

This note attempts to reinterpret these results in terms of the different influence of the vorticity on different baroclinic modes using a vertical normal mode analysis. Some preliminary findings using a linear approach are given in Section 2. Then two numerical experiments performed with a PE model in a spring and a fall situation, whose characteristics are close respectively to Rubenstein and Roberts' and Wang's situations, are briefly described in Section 3. The last section analyzes the velocity fields of these experiments in terms of the contribution of the different baroclinic modes in order to better understand the different spring and fall responses in light of the results of Section 2.

2. Vorticity effects on baroclinic modes

Let us consider the following linearized 2-D $(x - z)$ primitive equations that describe the response of the ocean to a wind impulse when a geostrophic barotropic

jet, $V(x)$, is present:

$$\begin{aligned} \frac{\partial u}{\partial t} - fv &= -\frac{\partial P}{\partial x} \\ \frac{\partial v}{\partial t} + f_e u &= 0 \\ \frac{\partial P}{\partial z} &= -\rho g \\ g\frac{\partial \rho}{\partial t} - N^2 w &= 0 \\ \frac{\partial u}{\partial x} + \frac{\partial w}{\partial z} &= 0 \end{aligned} \tag{1}$$

with

$$f_e = f + \frac{\partial V}{\partial x}$$

u, v and w are the horizontal and vertical velocity components; f is the Coriolis parameter and t the time. P is the pressure divided by density. ρ is the density perturbation from a state of rest for which the buoyancy frequency, N, is a given function of z. These equations can be reduced to only three equations involving the variables u, v and P. Let us expand these variables in terms of the vertical normal mode solutions, $\hat{p}_n(z)$, of the classical Sturm-Liouville problem:

$$\{u, v, P\} = \sum_{n=1}^{\infty} \{u_n, v_n, P_n\}\hat{p}_n(z) \tag{2}$$

where u_n, v_n and P_n depend only on x and t. The normal mode eigenfunctions satisfy:

$$\frac{\partial}{\partial z}\left(\frac{1}{N^2}\frac{\partial \hat{p}_n}{\partial z}\right) = -\frac{1}{c_n^2}\hat{p}_n, \tag{3}$$

where $c_n = R_n f$ with R_n the Rossby radius for mode n. Using (2) and (3), we get the following equation for u_n:

$$\frac{\partial^2 u_n}{\partial t^2} + ff_e u_n - c_n^2 \frac{\partial^2 u_n}{\partial x^2} = 0. \tag{4}$$

Some insights about the vorticity effects on the different baroclinic modes can be gained from the numerical integration of (4). The numerical model used is the same as the one and a half layer model described in Klein and Treguier (1993) with $f =$

10^{-4} s^{-1}. In the numerical experiment reported below, $V(x)$ is a cosine-like jet:

$$V(x) = V_o\left(1 + \cos\left(\frac{x}{L}\right)\right) \tag{5}$$

with $2\pi L = 80$ km and $V_o = 0.15$ m s^{-1} for $|x| < \pi L$ and 0 otherwise. This particular form of the jet does not affect the results insofar as the length scale L and the velocity at the jet center, $2V_o$, are not changed: numerical experiments performed with an exponential-like jet have displayed similar results. Initial conditions are $u_n = 0$ and $\partial u_n/\partial t = fv_i$ with $v_i = 0.2$ m s^{-1}. Two length scales are involved in this problem: L, the length scale of the geostrophic jet vorticity, and R_n, the Rossby radius of deformation associated with mode n. L is the appropriate length scale for the vorticity effects, while R_n is related to dispersion (through c_n). Results are shown on Figures 1 and 2 for two cases: one with $R_n/L = 0.25$, the other with $R_n/L = 1$.

The case with $R_n/L = 0.25$ (Fig. 1a) exhibits an asymmetric distribution of the inertial energy with a concentration on the negative vorticity side of the jet. After ten inertial periods, the ratio of kinetic energies $(E_{max} - E_{min})/E_{mean}$ attains a value close to 3.2. Frequency of the inertial motions is affected as well by the jet vorticity: after ten inertial periods, motions on the positive vorticity side are π out of phase with the negative vorticity side and $\pi/2$ out of phase with motions far from the jet (Fig. 1b). A physical explanation for this asymmetric inertial wave response in terms of horizontal dispersion has been given by Kunze (1985). Shift of the inertial wave frequency by the jet vorticity yields an increasing spatial variability of these waves characterized by a wavenumber ($k \approx -t/2\ \partial\zeta/\partial x$) across the front that is positive at the jet center and negative on the edges. As a consequence waves at the jet center are forced to propagate eastward while those on the edges propagate westward. Therefore the positive vorticity side becomes energy depleted while waves concentrate on the negative vorticity side (Fig. 1a). Results from other simulations (not shown) indicate that these features hold with smaller R_n except for the energy concentration which becomes smaller because of the lower horizontal propagation velocity, c_n.

The case $R_n/L = 1$ (Fig. 2a) strongly differs from the previous one. The energy is still larger on the right side of the jet but it is no longer concentrated in a narrow region. Instead it is dispersed well away from the jet and the ratio $(E_{max} - E_{min})/E_{mean}$ is lower (≈ 1.3) than before. A more astonishing feature, revealed by Figure 2b, is that the frequency of the inertial waves is very close to f and therefore appears to be unaffected by the vorticity effects, contrary to the preceding case. Other simulations performed with $R_n/L > 1$ (not shown) have displayed qualitatively the same results, the only difference is the smaller value of the ratio $(E_{max} - E_{min})/E_{mean}$ that, for example, attains 0.3 when $R_n/L = 2$.

These different vorticity effects on a baroclinic mode, depending on the ratio R_n/L, can be understood through an asymptotic analysis using L as a length scale, $1/f$ as a

time scale and v_i as a velocity scale. The parameter $\epsilon \equiv v_i/fL$, is usually very small. So let us consider the two limits: $R_n/L = \epsilon^{1/2}c$ and $R_n/L = \epsilon^{-1/2}c$ with $c = \mathcal{O}(1)$.

For the first limit, nondimensionalized Eq. (4) is:

$$\frac{\partial^2 u}{\partial t^2} + \omega^2 u - \epsilon c^2 \frac{\partial^2 u}{\partial x^2} = 0, \tag{6}$$

where all variables are now nondimensional and with $\omega^2(x) = 1 + \zeta(x)/f$. Using the truncated perturbation expansion in ϵ, $u = u_0 + \epsilon u_1$, solutions are:

$$u_0 = \frac{\sin(\omega t)}{\omega}, \qquad u_1 \approx \frac{c^2 t^2}{4\omega^2} \frac{\partial^2 \omega}{\partial x^2} \sin(\omega t). \tag{7}$$

Eq. (6) indicates that dispersion effects and therefore propagation of near-inertial waves are small in this case. Consequently these waves have time to be affected by the *local* jet vorticity and, using (7), their resulting dimensional frequency is f_e instead of f. This yields a spatial variability of the first order solution, u_0, characterized by a wavenumber across the front growing locally as $k \approx -t\partial\omega/\partial x$. Dispersion of this first-order solution forces a second-order motion, u_1, that *increases as* t^2 and is proportional to the second derivative of the vorticity. This explains the significant kinetic energy increase within the negative vorticity region and the decrease within the positive vorticity region. Amplitude of this variation also depends on c^2, indicating that this energy concentration should be smaller when R_n/L is smaller.

For the second limit, nondimensionalized Eq. (4) becomes:

$$\epsilon\left(\frac{\partial^2 u}{\partial t^2} + \omega^2 u\right) - c^2 \frac{\partial^2 u}{\partial x^2} = 0. \tag{8}$$

When boundary conditions are taken into account (motions are unaffected by the jet vorticity well away from the center), the zero- and first-order solutions are:

$$u_0 = \sin(t), \qquad u_1 \approx u_0 c^{-2} \int V(x)dx. \tag{9}$$

Eq. (8) shows that dispersion effects are now large and propagation of inertial waves is rapid. As a consequence the $\mathcal{O}(1)$ motions, u_0, are *not* affected by the jet vorticity and their frequency is equal to f. At the second order, the vorticity effects on the inertial motions $((\omega^2 - 1)u_0)$ are instantaneously compensated by dispersion that induces an $\mathcal{O}(\epsilon)$ motion, u_1, through the term $c^2(\partial^2 u_1/\partial x^2)$. The $\mathcal{O}(\epsilon)$ motion is spatially variable but *does not* increase with time. Its amplitude is proportional to c^{-2} and to the double integral of the vorticity. This explains the relatively larger kinetic energy that extends well away on the right side of the jet and the smaller one on the left side and that this energy amplitude difference is smaller when R_n/L (or c) is larger.

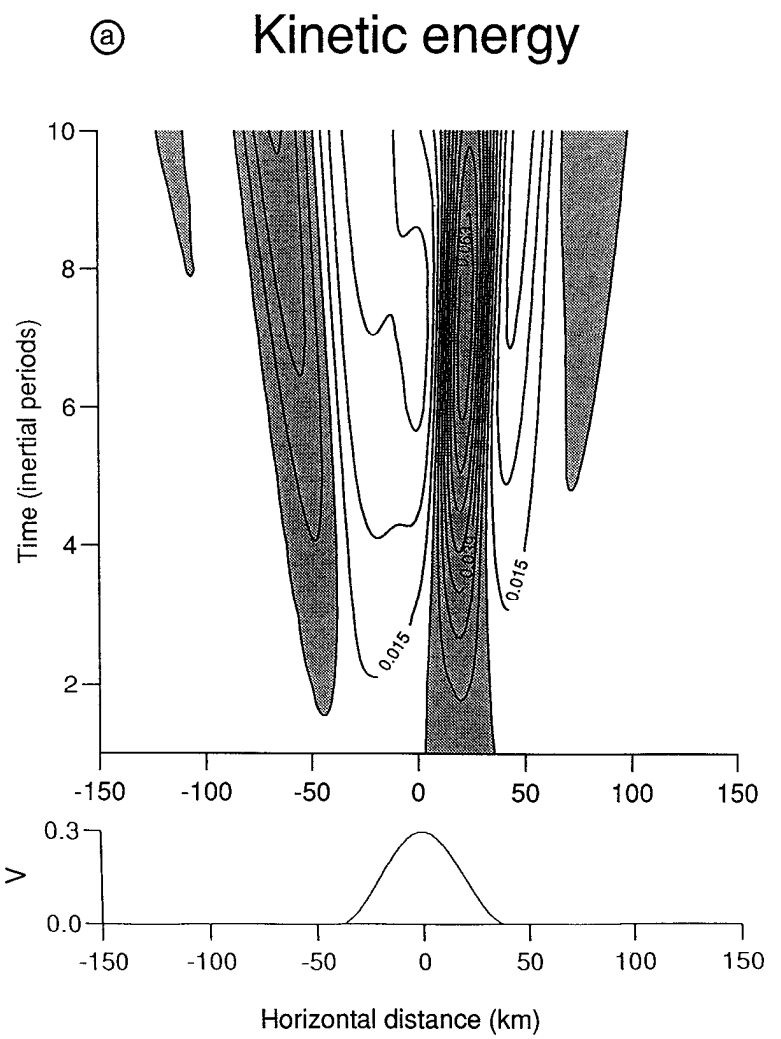

Figure 1. (a) Time-across-front plot of the kinetic energy (u^2) averaged over one inertial period with $R_n/L = 0.25$ and $\nu = 10$. Contour interval is 0.006 $m^2\ s^{-2}$ and regions with energy larger than 0.02 $m^2\ s^{-2}$ (mean value) are shaded. Velocity of the geostrophic jet (in m/s) is indicated below. (b) u-values at $x = -120$ km (continuous), $x = -20$ km (dashed-dotted), and $x = 20$ km (dotted).

3. Numerical experiments

A 2-D (x, z) nonlinear primitive-equation (PE) model is used to investigate the response of both the mixed layer and the ocean interior to a wind impulse. Stratification determines the horizontal and vertical propagation of the inertial waves below the mixed layer and therefore the distribution of kinetic energy in the ocean interior. Two realistic buoyancy Brünt-Väisälä profiles are considered (Fig. 3).

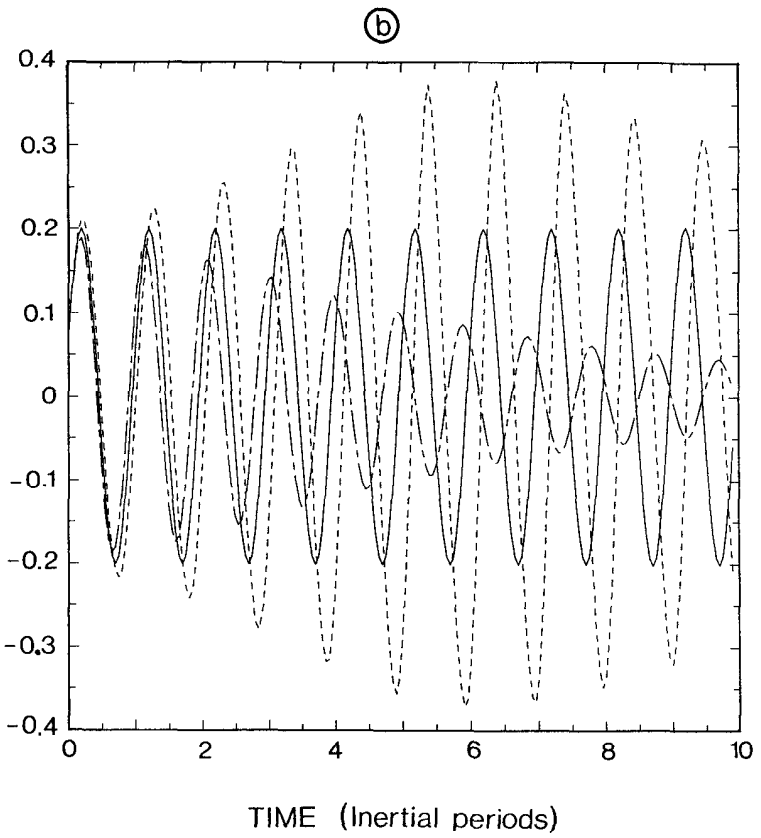

Figure 1. (Continued)

The first one characterizes spring conditions: a 10 m thick thermocline capped by a 26 m thick mixed layer. The second corresponds to fall conditions with a 100 m thick mixed layer above a 100 m thick thermocline. The wind impulse corresponds to a windstress of 2. 10^{-4} m^2 s^{-2} for spring and 6. 10^{-4} m^2 s^{-2} for fall, acting for half an inertial period so that the inertial motions have maximum amplitude when the wind stops. This impulse might result from the passage of a synoptic-scale atmospheric front. Characteristics of the spring and fall situations are close to the ones considered respectively by Rubenstein and Roberts (1986) and Wang (1991). We study the ocean response over 15 days, in the presence of the same barotropic geostrophic jet as considered in section 2. The 2-D PE model is described in Klein and Treguier (1993). It is based on the SPEM code (Haidvogel *et al.,* 1991) and uses a linear equation of state depending on temperature only. The rigid lid approximation is made. Finite differences are used in the horizontal and vertical. Turbulent fluxes are represented by diffusion for momentum and temperature, depending on the Richardson number following the classical level two model of Mellor and Yamada (1982).

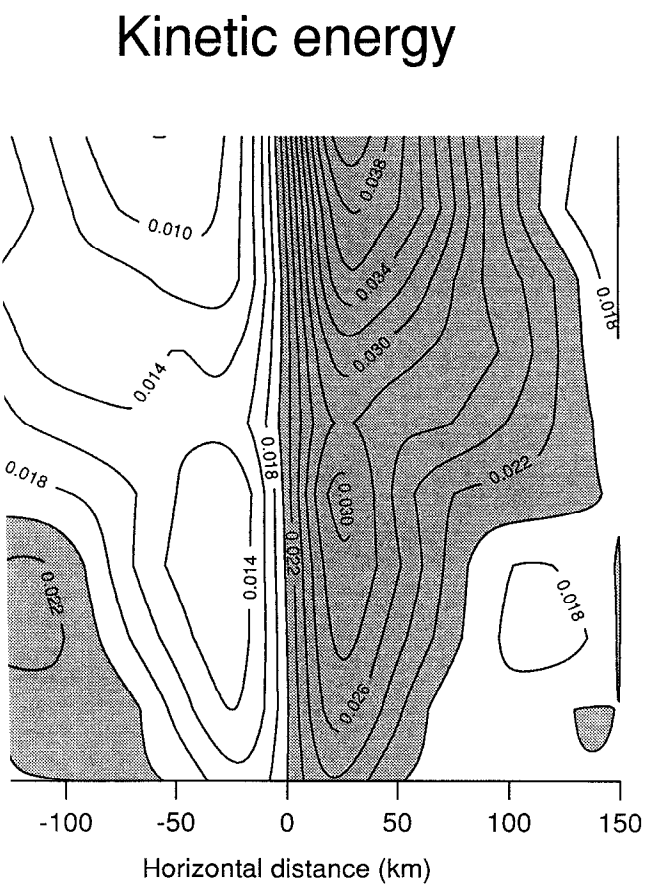

Figure 2. Same as Figure 1 but with $R_n = L$ and contour interval equal to 0.002 $m^2 s^{-2}$.

There are 114 levels in the vertical, with a grid spacing of 2 m down to 50 m depth, gradually increasing to reach 50 m at 1000 m depth, and then constant down to the bottom at 2000 m. The horizontal domain is 600 km wide with a grid spacing of 1.5 km. The time step is 300 s. There is a background vertical diffusion of 5. 10^{-5} $m^2 s^{-1}$ and a biharmonic horizontal friction equal to 10^8 $m^4 s^{-1}$ for momentum and temperature. Free slip conditions are used at the bottom.

a. Spring conditions. Time-evolution of the mixed layer kinetic energy (Fig. 4) displays the same qualitative features as Figure 1a; i.e., a significant concentration of inertial energy in the negative vorticity side and depletion on the positive vorticity side. Within the negative vorticity region, inertial energy attains a maximum of about 3 times its value outside the jet at $t \approx 5$ inertial periods. Time-evolution of the kinetic energy between 30 m and 2000 m (not shown) reveals that most of the downward energy propagation occurs within the negative vorticity region and remains trapped

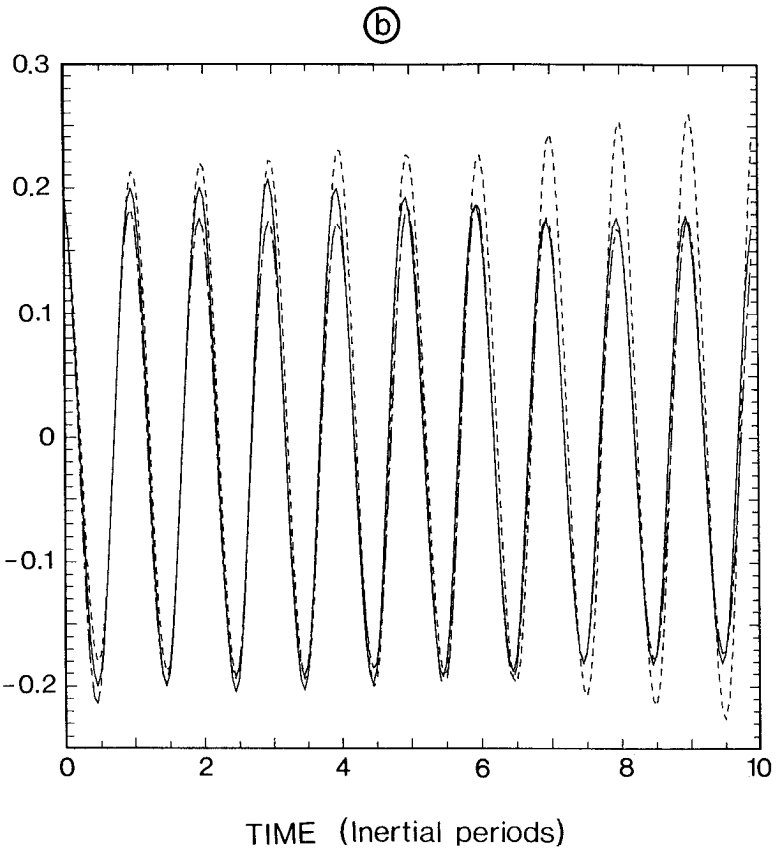

Figure 2. (Continued)

in this region. In both regions we have checked that the wave frequency is close to $f_e = \sqrt{f(f+\zeta)} \approx f + \zeta/2$, confirming that the frequency of the inertial motions is affected by vorticity.

b. Fall conditions. In the fall case, the mixed layer kinetic energy evolution (Fig. 5) displays a non-negligible energy concentration (depletion) in the negative (positive) vorticity side during the first three inertial periods. However, after six inertial periods, depletion of kinetic energy extends outside the positive vorticity region covering all the jet by 15 inertial periods. Time-evolution of the zonal velocity component within the mixed layer (not shown) indicates that frequency of these mixed layer motions is very close to f, i.e., very weakly affected by the jet vorticity. Time-evolution of the inertial waves in the positive and negative vorticity regions (Fig. 6) exhibits two large kinetic energy maxima building up within the thermocline on each side of the jet. A kinetic energy maximum first appears below the mixed layer

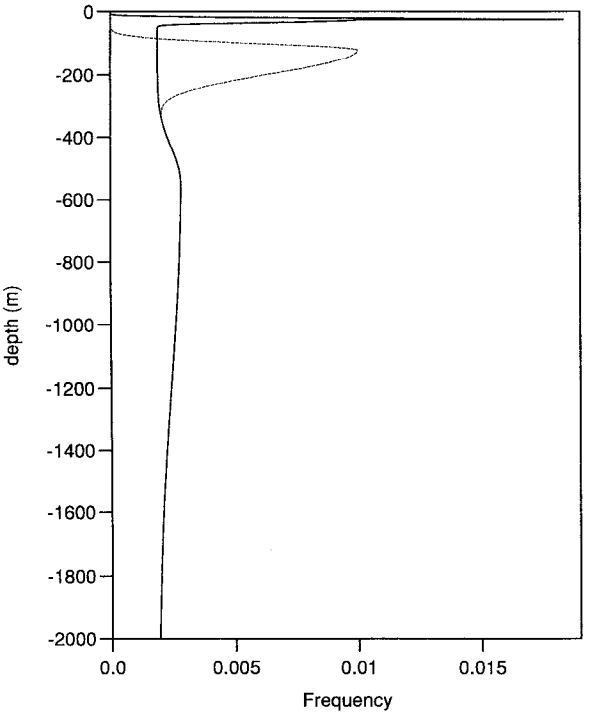

Figure 3. Initial vertical buoyancy frequency profiles ($N(z)$) used in simulations performed with the PE model. Solid (dashed) line describes spring (fall) conditions.

in the positive vorticity region (Fig. 6a). In the negative vorticity region, kinetic energy below the mixed layer increases but remains smaller than that within the mixed layer (Fig. 6b). Later the maximum in the positive vorticity region shrinks and a thick maximum appears in the negative vorticity region and keeps growing. Furthermore Figure 6 indicates that below the mixed layer, near-inertial motions, during the first inertial periods, have *downward* phase propagation in the positive vorticity region. Classical upward phase propagation is observed in the negative vorticity region. These results are quite similar to those of Wang (1991) although the geostrophic jet considered here is barotropic.

4. Vertical normal-modes analysis

In order to investigate the mechanisms involved in the near-inertial wave dynamics we performed other simulations with the same PE model but with the linearized equations: all nonlinear advection terms have been dropped except jet vorticity in the equation for v and vertical advection of the background density in the density equation. Results over 20 inertial periods were virtually identical! Consequently wave-wave interactions have negligible effects. This, with the fact that the jet is

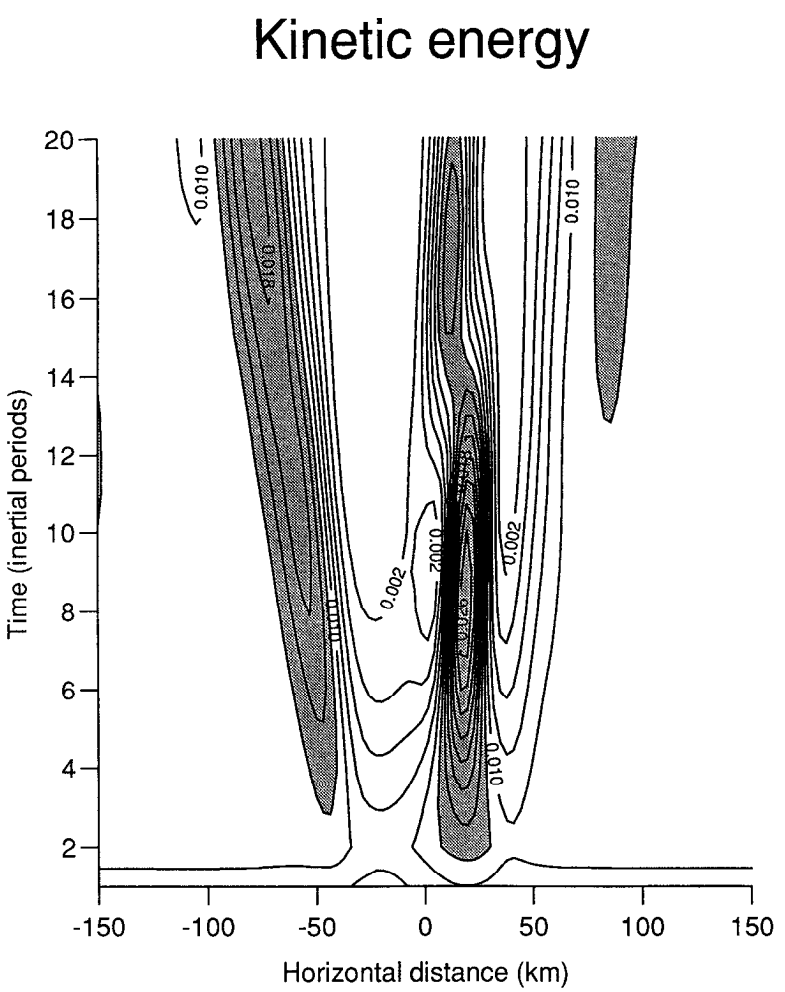

Figure 4. Time-acrossfront plots of the kinetic energy (u^2) corresponding to spring conditions. Kinetic energy is averaged over one inertial period and averaged over the top layer (0–30 m). Contour interval is 0.002 $m^2\ s^{-2}$ and regions with energy larger than 0.0115 $m^2\ s^{-2}$ (mean value) are shaded.

barotropic, allows us to analyze the numerical results of the PE model using vertical normal modes (Pollard, 1970 and Gill, 1984) to better understand the characteristic features of the preceding numerical experiments in terms of the different baroclinic modes contributions. This analysis has revealed that in the spring case motions are captured by baroclinic modes with Rossby radius wavelengths equal to or smaller than 20 km, i.e., a scale smaller than the geostrophic vorticity wavelength (80 km). The lower modes are much less energetic. This explains the similarity of Figure 1a and Figure 4. In the fall case the lowest modes (with Rossby radii close to or larger

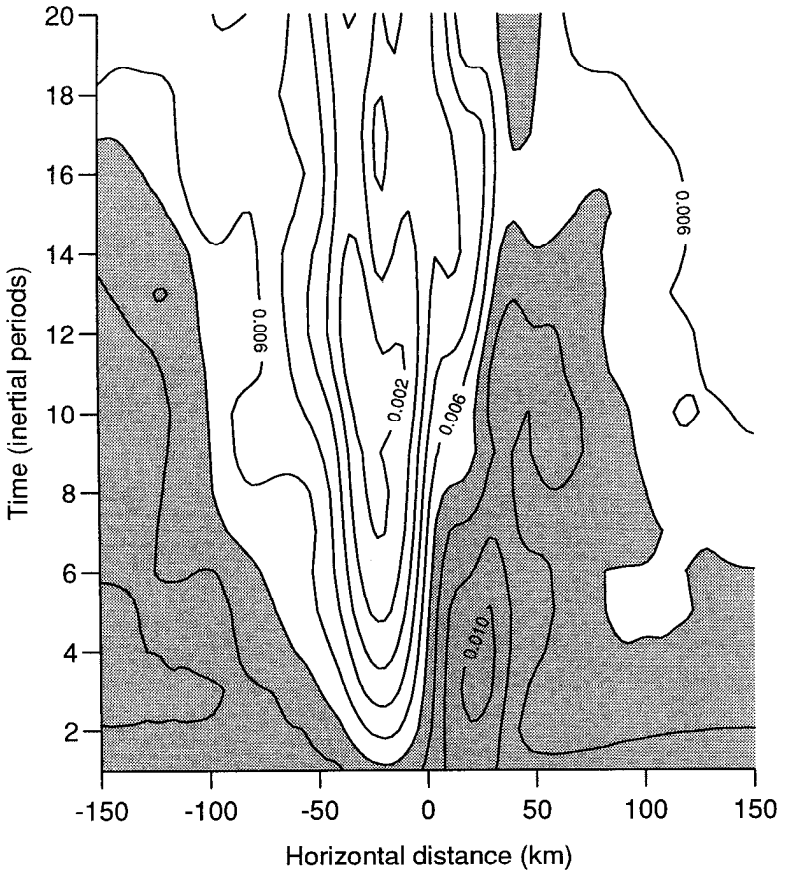

Figure 5. Time-across-front plots of the kinetic energy (u^2) corresponding to fall conditions. Kinetic energy is averaged over one inertial period and averaged over the top layer (0–100 m). Contour interval is 0.001 $m^2\ s^{-2}$ and regions with energy larger than 0.008 $m^2\ s^{-2}$ (mean value) are shaded.

than the vorticity length scale) are at least as energetic as the higher modes. We have found that the competition of these lowest baroclinic modes with the higher ones explains the differences between the spring and fall cases. This competition is examined and discussed in the next sections in the light of the results of Section 2.

a. Modal analysis of the fall case. Time and space evolution of the zonal velocity component of the inertial waves is examined at two locations: in the positive (x = 20 km) and negative (x = −20 km) vorticity regions. When the wind stops (at $t = \pi/f$), numerical results show that u is nonzero in the mixed layer ($u = u_o$) and zero below. Consequently we rewrite the u-field at each location as

$$u(x, z, t) = u_o S(x, z, t). \tag{10}$$

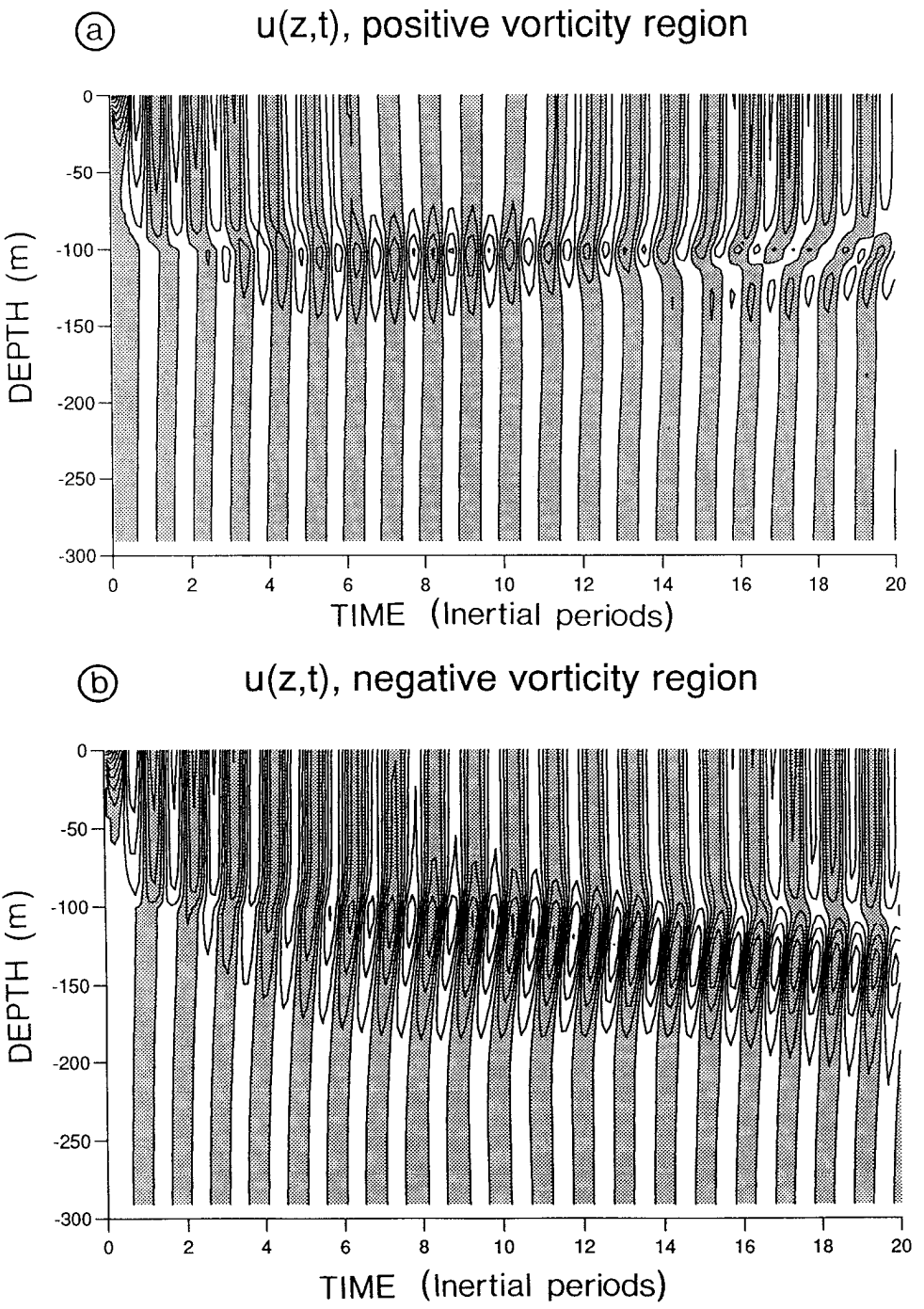

Figure 6. Time-evolution of the cross-frontal velocity profile (a) at $x = -20$ km, (b) at $x = 20$ km. Grey indicates positive velocities. Contour interval is 0.05 m s^{-1}.

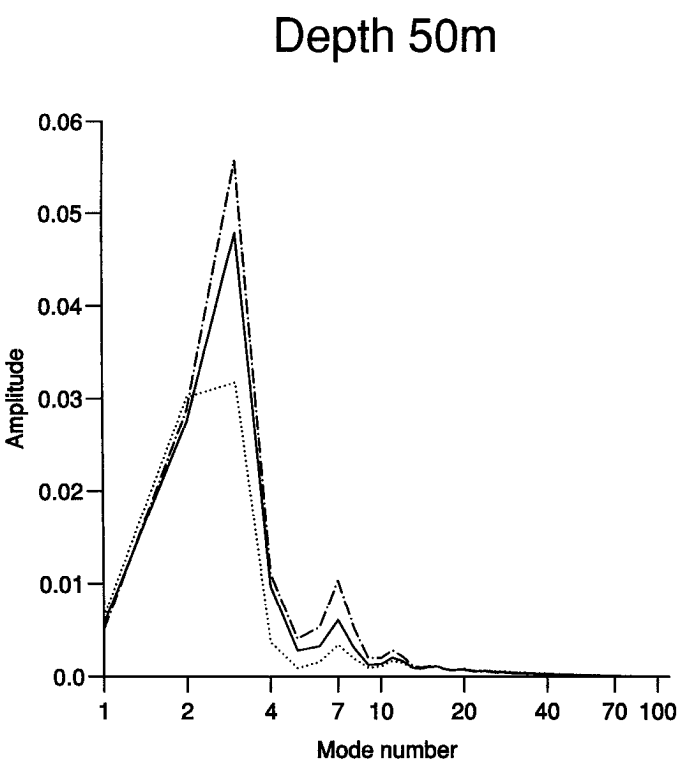

Figure 7. Spectrum of the velocity field, u, at $x = -120$ km (—), $x = -20$ km (···), $x = 20$ km (—·—) for three depths.

where $S(x, z, \pi/f)$ is equal to 1 in the mixed layer and 0 below. Time-evolution of $S(x, z, t)$, that is entirely determined from $u(x, z, t)$, is then expanded in normal modes $\hat{p}_n(z)$:

$$S(x, z, t) = \sum_{n=1}^{N} \sigma_n(x, t)\hat{p}_n(z). \tag{11}$$

Normal modes have been calculated from the buoyancy frequency profiles of Figure 3. $\sigma_n(x, t)$ is calculated by projecting the numerical solution $u(x, z, t)$ of the PE model onto up to 110 modes ($N = 110$).

Figure 7 displays the maximum amplitude of each $\sigma_n(x,t)\hat{p}_n(z)$ between the fifth and seventh inertial periods at three depths and at three x-locations. At a given depth the $\sigma_n(x,t)\hat{p}_n(z)$ spectra display the same shape at the three x-locations. More than 90% of the variance is captured by the first 100 modes. Moreover examination of these spectra at different times (not shown) has revealed the same features. This makes us confident about the number of modes considered. At all depths and x-locations modes 4 and 5 as well as modes 9 and 10 are always weak. Therefore we

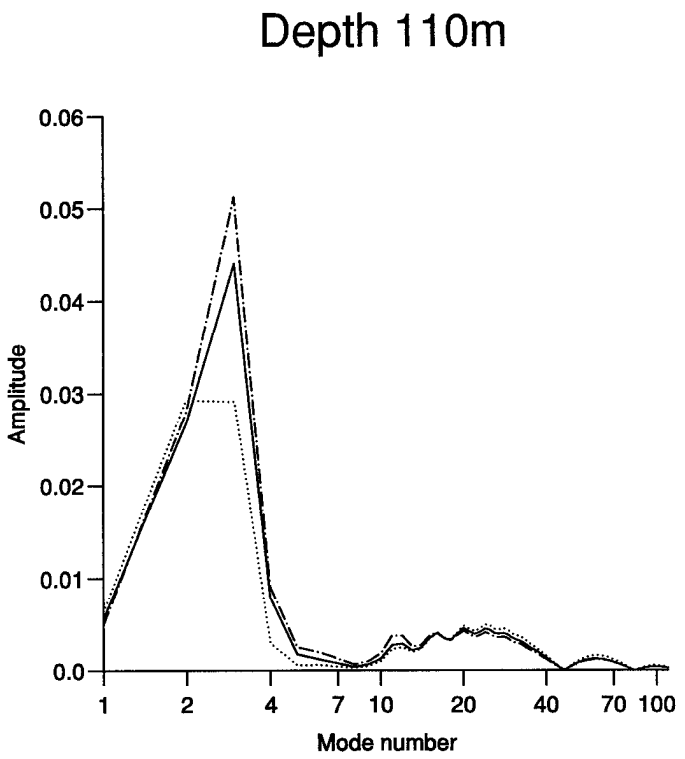

Figure 7. (Continued)

define three classes: the lowest modes ($n = 2, 3$) whose Rossby radius wavelengths ($2\pi R_n$) are respectively 100 km and 60 km, the intermediate modes ($4 \leq n < 9$) with Rossby radii close to 20 km and the highest modes ($n \geq 10$) with Rossby radii equal to or lower than 12 km. The barotropic mode ($n = 1$) is always negligible. Consequently $S(x, z, t)$ is rewritten as:

$$S(x, z, t) = S_1(x, z, t) + S_2(x, z, t) + S_3(x, z, t) \tag{12}$$

where $S_1(x, z, t) = \Sigma_{n=2}^{3}\sigma_n(x, t)\hat{p}_n(z)$, $S_2(x, z, t) = \Sigma_{n=4}^{9}\sigma_n(x, t)\hat{p}_n(z)$ and $S_3(x, z, t) = \Sigma_{n=10}^{110}\sigma_n(x, t)\hat{p}_n(z)$ represent the contributions of the lowest, intermediate and highest modes respectively.

Vertical profiles of the different mode contributions just after the wind impulse ($t = \pi/f$) are shown on Figure 8. Within the mixed layer the lowest baroclinic modes that are the dominant ones are in phase with the other modes. At $z = -110$ m, i.e., just below the mixed layer, the lowest modes and the highest modes dominate and are just π out of phase. Within the thermocline (at $z = -150$ m) the lowest and intermediate modes dominate and are also just π out of phase. These compensations explain the zero velocity below the mixed layer at $t = \pi/f$. Time evolution of S_1, S_2

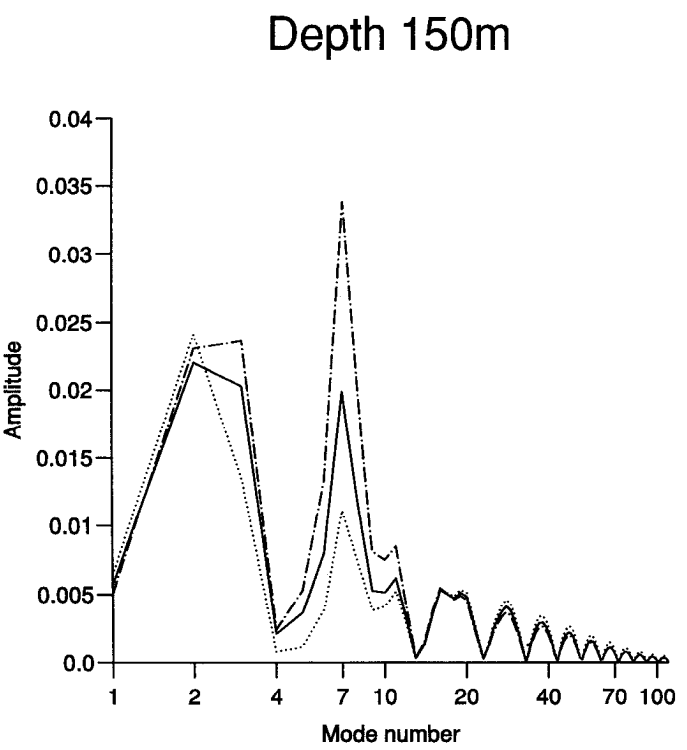

Figure 7. (Continued)

and S_3 is shown for the positive (Fig. 9) and negative (Fig. 10) vorticity regions. Close examination of the first eight inertial periods reveals that frequency of the lowest modes is almost equal to the inertial frequency f and therefore is not affected by vorticity. On the other hand, the intermediate and highest modes frequencies are close to $f_e \approx f + \zeta/2$. This is illustrated in Figures 9a and 10a: S_1 and S_3, initially in phase, become π out of phase at $t = 8.3$ inertial periods. S_3 has experienced nine cycles in the $\zeta > 0$ region (Fig. 9a) and only eight cycles in the $\zeta < 0$ region (Fig. 10a), while evolution of S_1 is identical in both regions. Maximum amplitudes of S_1 and S_3 display very weak variations with time. One noteworthy feature is that the amplitude of S_1 is larger on the negative vorticity side whereas that of S_3 is the same in both negative and positive vorticity regions. On the other hand, the amplitude of S_2 decreases (increases) with time in the positive (negative) vorticity region.

b. Discussion. The behaviors of the different modes described above compare well with the findings of Section 2 when these modes are classified with respect to their Rossby radius versus the vorticity length scale. The lowest baroclinic modes S_1, having their Rossby radius wavelength close to the vorticity wavelength ($2\pi L = 80$ km), behave as found in Section 2 for the modes characterized by $R_n/L \geq$

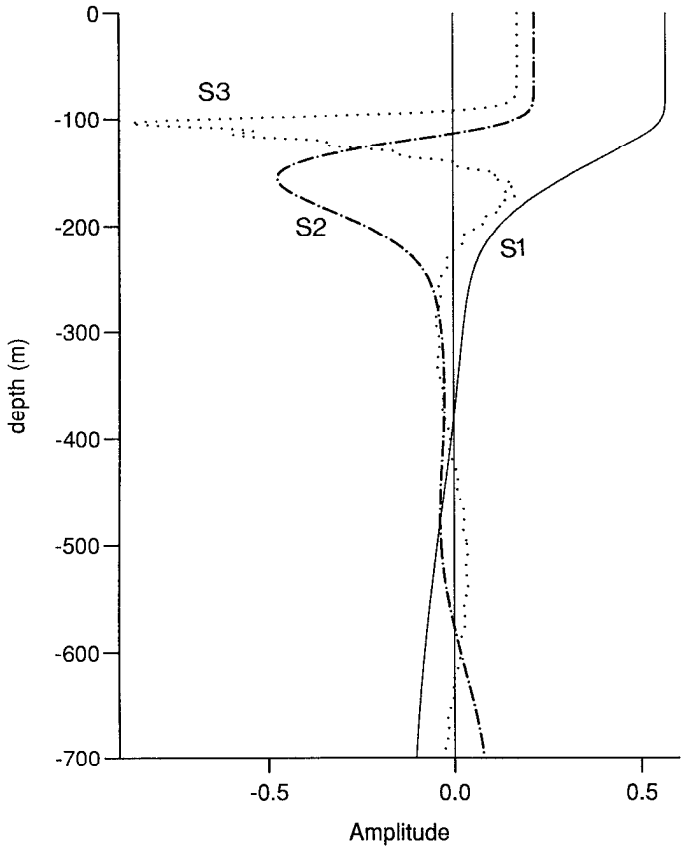

Figure 8. Vertical profiles of the S_1 (—), S_2 (—·—) and S_3 (----) at $t = \pi/f$ for fall conditions.

(1): their frequency is very close to f and their amplitude (slightly larger on the negative vorticity side) does not change much with time. On the other hand the intermediate and highest modes, S_2 and S_3, have their Rossby radii smaller than the vorticity length scale, i.e., $R_n/L < 1$. Referring to the findings of Section 2, the very small Rossby radius of the highest modes explains the fact that these modes are very weakly affected by horizontal dispersion effects as shown by their almost steady amplitude (with the same value on both sides of the jet) although their frequency is shifted by the jet vorticity. The frequency of the intermediate modes is affected by the jet vorticity as well (since $R_n/L < 1$), but the large variation of their amplitude is explained by their larger Rossby radii that increase the dispersion effects.

Let us now explain the subsurface maxima and the anomalous vertical phase propagation in terms of competition between the different baroclinic modes. At $t = \pi/f$ lowest modes balance the highest or intermediate ones below the mixed layer. This yields a zero velocity there. As time goes on, near-inertial waves propagate

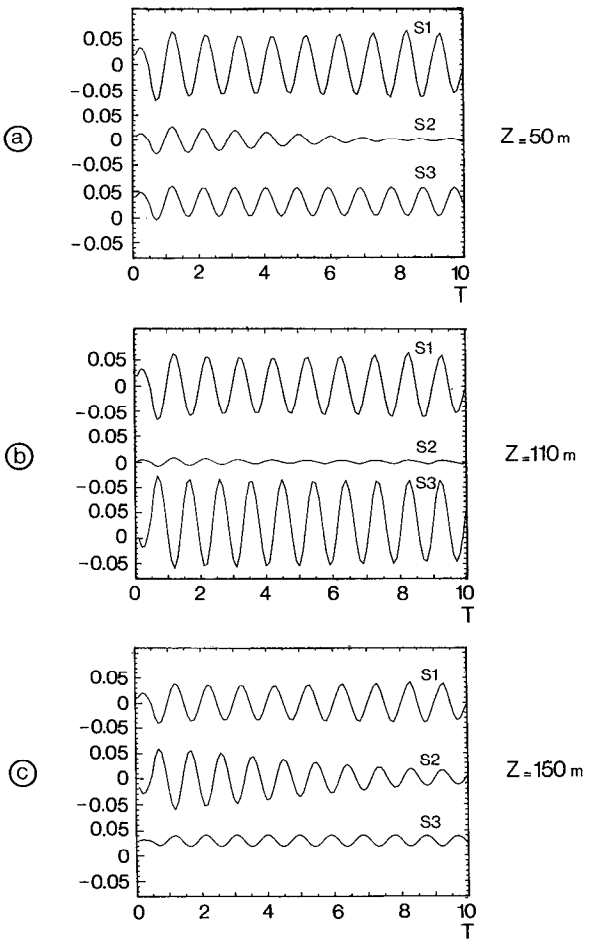

Figure 9. Time-evolution of the S_m's functions during fall in the positive vorticity region at (a) $z = 50$ m, (b) $z = 110$ m, (c) $z = 150$ m.

downward and the velocity becomes non-zero. This mechanism can be interpreted in terms of time evolution of the baroclinic modes as follows (Gill, 1984): each mode has a frequency that slightly differs from the others. Consequently a phase shift between the modes builds up with time, which leads to the appearance of a non-zero velocity below the mixed layer. Characteristic features revealed in fall conditions can then be explained as follows:

The frequency observed within the mixed layer, close to f (see Fig. 6), is due to dominance of the lowest modes (S_1). The relative kinetic energy depletion in the mixed layer is caused by an increasing phase shift between the low and higher modes because of their different frequencies (Figs. 9a and 10a). The larger and more rapid

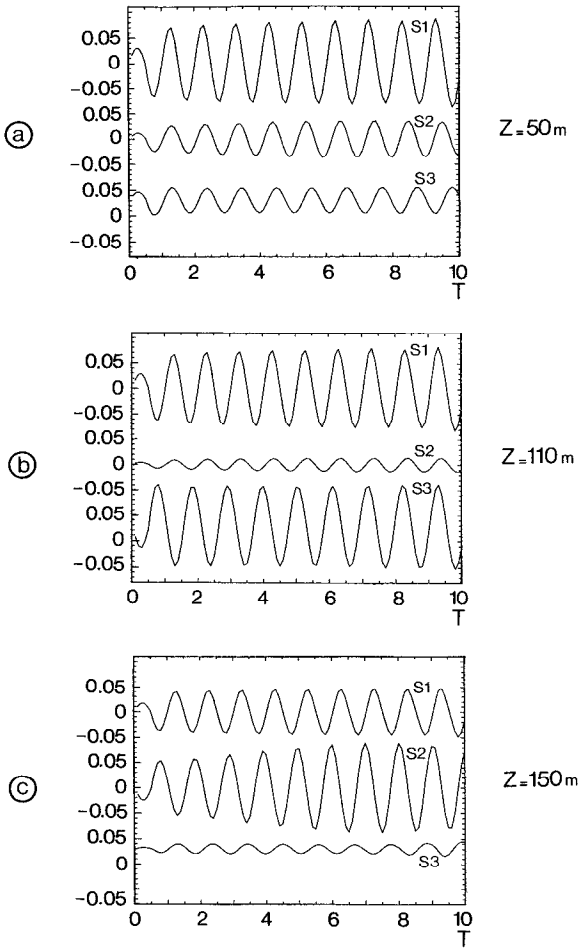

Figure 10. Time-volution of the S_m's functions during fall in the negative vorticity region at (a) $z = 50$ m, (b) $z = 110$ m, (c) $z = 150$ m.

kinetic energy depletion in the positive vorticity region is due to the horizontal propagation of the intermediate modes (S_2) away from this region.

Below the mixed layer, the increasing phase shift between the low and higher modes leads to the appearance of near-inertial motions and the build-up of the two maxima. This phase shift also explains the vertical phase propagation during the first inertial periods. Letting f be the frequency of the lowest modes that dominate within the mixed layer and $f_e \approx f + \zeta/2$ the frequency of the higher modes that balance the lowest ones below the mixed layer, mixed layer (u_{ml}) and deep velocities (u_b) can be written: $u_{ml} = u_o \cos(ft)$ and $u_b = u_o(\cos(ft) - \cos(f_e t))$. Assuming $f \approx f_e$ (or $\zeta/f \ll 1$) leads to: $u_b \approx u_o|\zeta/2|t \cos(-\pi/2 + ft)$ if $\zeta > 0$ and $u_b \approx u_o|\zeta/2|t \cos(\pi/2 + ft)$ if $\zeta < 0$. Thus, as illustrated in Figure 11, during the first inertial

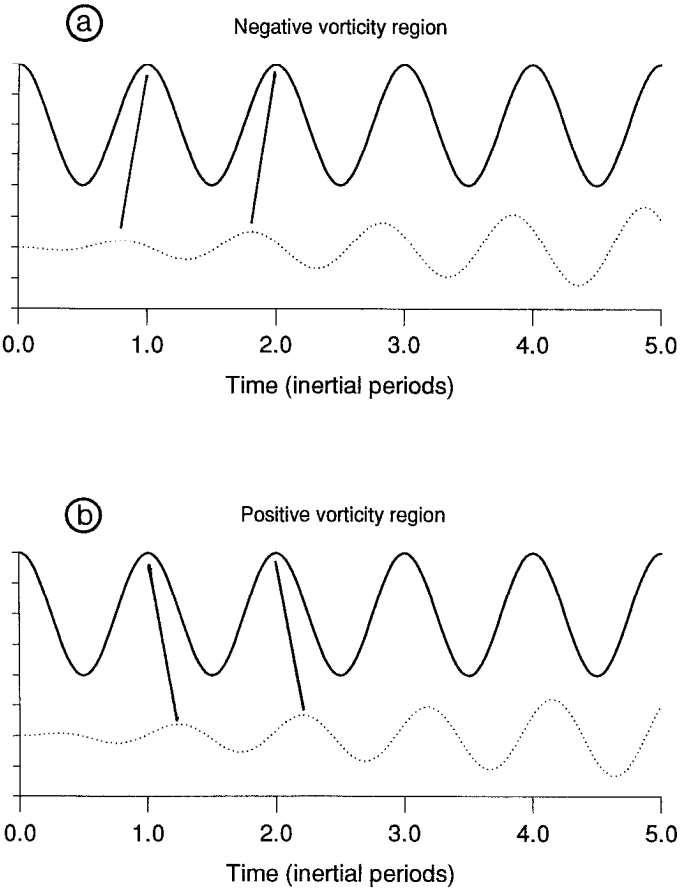

Figure 11. Illustration of the apparent vertical phase propagation in (a) the negative vorticity region (with $f_e < f$) and (b) the positive vorticity region (with $f_e > f$). In each region two curves are shown: $\cos(ft)$ (continuous line) representing the velocity in the mixed layer and $(\cos(ft) - \cos(f_e t))$ (dotted line) the velocity below.

period there is a shift of $-\pi/2$ (upward phase propagation) when $f > f_e$, i.e. in the negative vorticity region. On the other hand there is a phase shift of $\pi/2$, i.e. an anomalous downward phase propagation in the positive vorticity region (where $f < f_e$). It is the sign of the difference between the frequency of the lowest modes (dominating the mixed layer) and higher modes that determines the sign of the vertical phase propagation. As time goes on, the deepening (shrinking) of the kinetic energy maximum in the negative (positive) vorticity region (Fig. 6), is attributed to the horizontal dispersion effects of intermediate modes that are the dominant modes within the thermocline (Figs. 9c and 10c).

5. Conclusion

In this study we have re-examined the dispersion of wind-induced inertial waves by an oceanic geostrophic jet. It is shown that the nonlinear wave-wave interactions do not qualitatively affect the mixed layer response nor the propagation of the near-inertial waves into the thermocline and the ocean interior. In other words, most of the dynamics of the free near-inertial waves is captured by the linearized equations. This has allowed us to use a vertical normal mode approach to analyze the numerical results from a primitive equations model.

A simple analytical model has revealed that vorticity effects on a baroclinic mode strongly depend on the ratio of its Rossby radius with the vorticity length scale. When this ratio is small, dispersion effects are small and the inertial waves are significantly affected by the local jet vorticity. As shown by Kunze (1985) and Rubenstein and Roberts (1986) the resulting wavenumber growing across the front induces a local asymmetric dispersion that significantly concentrates inertial energy in the negative vorticity region. On the other hand when this ratio is of order $O(1)$ or larger, the large dispersion effects efficiently overcome the vorticity effects so that the resulting spatial variability of the inertial waves is small and does not increase with time. To our knowledge this result, although not surprising, has not been reported in the literature.

We have assessed the consequences on the dispersion by a barotropic jet of a wind-induced inertial wave field, initially homogeneous and entirely contained within the mixed layer, in two different realistic situations. Results indicate that, for a buoyancy Brunt-Väisälä profile corresponding to a spring situation (characterized by a shallow mixed layer capping a thin thermocline), inertial energy rapidly concentrates within the negative vorticity region. These results are in agreement with the preceding findings since a vertical normal mode analysis reveals that the inertial wave field energy is almost entirely captured by baroclinic modes whose Rossby radius is smaller than the vorticity length scale. On the other hand, when the buoyancy Brunt-Väisälä profile corresponds to a fall situation (with a deep mixed layer capping a thick thermocline) horizontal and vertical dispersion of the near-inertial waves differs from the preceding situation and is close to the one reported by Wang (1991). Two distinct inertial energy maxima are found within the stratified interior, associated with a classical upward phase propagation of the near-inertial waves in the negative vorticity region and an anomalously downward phase propagation in the positive vorticity region. The vertical normal modes analysis clarifies these results. In this situation baroclinic modes with a Rossby radius close to the vorticity length scale capture a significant part of the inertial wave energy. These modes are not affected by the vorticity contrary to the higher modes. It is the competition between these two classes of baroclinic modes that lead to the characteristic features observed in the fall situation.

These results indicate that dispersion of the wind-induced inertial waves strongly depends on the mixed layer depth and on the stratification underneath.

Acknowledgments. This work is supported by IFREMER and the CNRS. Some of the calculations reported here were done at the Centre de Calcul Vectoriel pour la Recherche (Palaiseau, France). The authors acknowledge the valuable comments and suggestions of both reviewers which led to substantial improvement in the manuscript.

REFERENCES

Gill, A. E. 1984. On the behavior of internal waves in the wakes of storms. J. Phys. Oceanogr., *14,* 1129–1151.

Haidvogel, D. B., J. L. Wilkin and R. Young. 1991. A semi-spectral primitive equation ocean circulation model using vertical sigma and orthogonal curvilinear horizontal coordinates. J. Comp. Phys., *94,* 151–185.

Klein, P. and A. M. Treguier. 1993. Inertial resonance induced by a geostrophic jet. J. Phys. Oceanogr., *23,* 1897–1915.

Kunze, E. 1985. Near-inertial wave propagation in geostrophic shear. J. Phys. Oceanogr., *15,* 544–565.

Mellor, G. L. and T. Yamada. 1982. Development of turbulence closure model for geophysical fluid problems. Rev. Geophys. Space Phys., *20,* 851–875.

Pollard, R. T. 1970. On the generation by winds of inertial waves in the ocean. Deep-Sea Res., *17,* 795–812.

Rubenstein, D. H. and G. O. Roberts. 1985. Scattering of inertial waves by an ocean front. J. Phys. Oceanogr., *16,* 121–131.

Treguier, A. M. and P. Klein. 1994. Instability of wind-forced inertial oscillations. J. Fluid Mech. *275,* 323–349.

Wang, D. P. 1991. Generation and propagation of inertial waves in the subtropical front. J. Mar. Res. *49,* 619–663.

Received: *20 July, 1993;* revised: *21 June, 1994.*